This article may be downloaded for personal use only. Any other use requires prior permission of the author and AIP Publishing. This article appeared in P. Schütz, M. Kamp, D. Di Sante, A. Lubk, B. Büchner, G. Sangiovanni, M. Sing, and R. Claessen, Electronic structure of epitaxial perovskite films in the two-dimensional limit: Role of the surface termination, Appl. Phys. Lett. 116, 201601 (2020) *and may be found at* https://doi.org/10.1063/5.0002985

Applied Physics Letters

Electronic structure of epitaxial perovskite films in the two-dimensional limit: Role of the surface termination

Cite as: Appl. Phys. Lett. **116**, 201601 (2020); https://doi.org/10.1063/5.0002985
Submitted: 29 January 2020 . Accepted: 17 April 2020 . Published Online: 18 May 2020

P. Schütz, M. Kamp, D. Di Sante, A. Lubk, B. Büchner, G. Sangiovanni, M. Sing, and R. Claessen

COLLECTIONS

F This paper was selected as Featured

SCI This paper was selected as Scilight

View Online Export Citation CrossMark

ARTICLES YOU MAY BE INTERESTED IN

Spinwave detection by nitrogen-vacancy centers in diamond as a function of probe-sample separation
Applied Physics Letters **116**, 202401 (2020); https://doi.org/10.1063/1.5141921

Understanding the electronic behavior of iridium-based perovskites
Scilight **2020**, 211101 (2020); https://doi.org/10.1063/10.0001303

Oxygen vacancies: The (in)visible friend of oxide electronics
Applied Physics Letters **116**, 120505 (2020); https://doi.org/10.1063/1.5143309

New
SHFQA
Quantum Analyzer
8.5 GHz
Zurich Instruments
Your Qubits. Measured.
Meet the next generation of quantum analyzers
Readout for up to 64 qubits
Operation at up to 8.5 GHz, mixer-calibration-free
Signal optimization with minimal latency
Find out more
Zurich Instruments

© 2020 Author(s).

Applied Physics Letters ARTICLE scitation.org/journal/apl

Electronic structure of epitaxial perovskite films in the two-dimensional limit: Role of the surface termination

Cite as: Appl. Phys. Lett. **116**, 201601 (2020); doi: 10.1063/5.0002985
Submitted: 29 January 2020 · Accepted: 17 April 2020 ·
Published Online: 18 May 2020

P. Schütz,[1] M. Kamp,[1] D. Di Sante,[2] A. Lubk,[3] B. Büchner,[3] G. Sangiovanni,[2] M. Sing,[1,a)] and R. Claessen[1]

AFFILIATIONS

[1] Physikalisches Institut and Würzburg-Dresden Cluster of Excellence ct.qmat, Universität Würzburg, D-97074 Würzburg, Germany
[2] Institut für Theoretische Physik und Astrophysik and Würzburg-Dresden Cluster of Excellence ct.qmat, Universität Würzburg, D-97074 Würzburg, Germany
[3] IFW Dresden and Würzburg-Dresden Cluster of Excellence ct.qmat, D-01069 Dresden, Germany

[a)] Author to whom correspondence should be addressed: sing@physik.uni-wuerzburg.de

ABSTRACT

An often-overlooked property of transition metal oxide thin films is their microscopic surface structure and its effect on the electronic properties in the ultrathin limit. Contrary to the expected conservation of the perovskite stacking order in the (001) direction, heteroepitaxially grown $SrIrO_3$ films on TiO_2-terminated $SrTiO_3$ are found to exhibit a terminating SrO surface layer. The proposed mechanism for the self-organized conversion involves the adsorption of excess oxygen ions at the apical sites of the IrO_2-terminated surface and the subsequent decomposition of the IrO_6 octahedra into gaseous molecular IrO_3 and the remaining SrO-terminated surface. Whereas the *ab initio* calculated electronic structure of SrO-terminated $SrIrO_3$ in the monolayer limit exhibits a striking similarity to bulk Sr_2IrO_4, the broken octahedral symmetry at the IrO_2-terminated surface would mix the otherwise crystal field split e_g and t_{2g} states, resulting in distinctly different low-energy electronic states.

Published under license by AIP Publishing. https://doi.org/10.1063/5.0002985

In the last decade, iridates have moved into the focus of solid state research since the interplay between the comparably strong Coulomb and spin–orbit interactions in their 5*d* orbitals is expected to result in hitherto-unforeseen properties.[1] The Ruddlesden–Popper (RP) family of strontium iridates $Sr_{n+1}Ir_nO_{3n+1}$ has attracted special attention due to the observation of an exotic spin–orbit entangled Mott insulating ground state in its quasi-two-dimensional end member Sr_2IrO_4 $(n = 1)$[2,3] and the phenomenological similarities to the high-T_C cuprate superconductors upon doping.[4,5] In contrast to its layered counterparts (n = 1, 2), the three-dimensional $n = \infty$ RP phase $SrIrO_3$ is thermodynamically metastable at ambient conditions and can only be synthesized in polycrystalline form upon the application of high pressure and temperature.[6,7] In an alternative approach, the perovskite phase can be stabilized in a thin-film geometry by effectively substituting the external pressure with epitaxial strain to an underlying substrate. The resulting $SrIrO_3$ films adopt a distorted perovskite structure,[8,9] which is predicted to support topologically non-trivial zero-energy surface states protected by chiral and mirror-reflection symmetries.[10,11] Upon transition into the two-dimensional limit, $SrIrO_3$ thin films undergo a metal-insulator transition and adopt an electronic structure that closely resembles that of bulk Sr_2IrO_4.[9,12] A deeper understanding of the microscopic aspects of this behavior requires in-depth knowledge of the crystallographic structure of not only the bulk but also the surface of $SrIrO_3$ films. In this Letter, we provide evidence for the conversion from an IrO_2 to a SrO surface termination during the growth of $SrIrO_3$ on TiO_2-terminated $SrTiO_3$ as a consequence of the thermodynamic instability of the topmost IrO_2 layer. The pronounced effects on the electronic structure of $SrIrO_3$ in the monolayer limit are investigated by *ab initio* band structure calculations.

Pulsed laser deposition (PLD) is a commonly employed technique for the heteroepitaxy of ternary oxides. Two of the major challenges for the synthesis of high-quality specimens are the stoichiometric transfer of the different atomic species from the target to the substrate and the control of the oxidative state of the transition metal cation. The former is not trivial and critically depends on the respective atomic masses and details of the ablation process (e.g., laser fluency, repetition rate, scanned ablation area,…),[13–17] whereas the latter primarily depends on the type and pressure of the provided background gas (e.g., O_2, O_3, Ar, NO_2,…).[18–20] These challenges may become strongly intertwined if the transition metal forms a volatile gaseous compound upon over-oxidation. This is the case for PLD growth of $SrRuO_3$ and $SrIrO_3$, where excessive temperature and/or oxygen partial pressure may result in the formation of volatile RuO_3/RuO_4[21] and IrO_3,[22,23] respectively. Using a stoichiometric $SrRuO_3$ ($SrIrO_3$) target, the substantial loss of ruthenium (iridium) may, therefore, lead to the growth of the RP phases $Sr_3Ru_2O_7$ or Sr_2RuO_4[24] ($Sr_3Ir_2O_7$ or Sr_2IrO_4[25]) Indeed, it has been shown that the growth phase diagram can be mapped onto the phase diagram expected from thermodynamic equilibrium despite the inherent non-equilibrium nature of pulsed laser deposition.[25]

Here, we investigate the microstructure of strontium iridate thin films with varying degrees of iridium deficiency and the types of structural lattice faults therein. For this purpose, strontium iridate films are heteroepitaxially grown on (001)-oriented TiO_2-terminated $SrTiO_3$ substrates[26,27] by pulsed laser deposition from a polycrystalline target composed of stoichiometric 6H-$SrIrO_3$ in its thermodynamically stable hexagonal polymorphic form.[6,7] The films were grown at variable substrate temperatures and structurally investigated by a combination of out-of-plane x-ray diffraction (XRD) using a Cu K_α-source and scanning transmission electron microscopy in high-angle annular dark field mode (HAADF-STEM). Density functional theory calculations were performed by using the VASP *ab initio* simulation package[28] within the projector-augmented-plane wave (PAW) method,[29,30] using the generalized gradient approximation (GGA), as parametrized by the PBE GGA functional.[31] Spin–orbit coupling was self-consistently included,[32] and the Coulomb repulsion U and exchange interaction J of Ir d orbitals were treated within the rotationally invariant density functional theory (DFT) + U scheme of Liechtenstein.[33]

The strontium iridate RP compounds $Sr_{n+1}Ir_nO_{3n+1}$ = ($[SrIrO_3]_n$,SrO) essentially consist of n $SrIrO_3$ perovskite layers that are intercalated by SrO layers and laterally shifted against each other such that no Ir–O–Ir bonds persist between neighboring $[SrIrO_3]_n$ blocks. Figures 1(a)–1(c) show HAADF-STEM images of a strontium iridate film grown at a substrate temperature of 820 °C from a $SrIrO_3$ target. In agreement with the out-of-plane XRD pattern shown in Fig. 1(d), the lattice structure predominantly exhibits the $n = 2$ RP phase $Sr_3Ir_2O_7$. As highlighted in the inset of Fig. 1(a), the neighboring bilayers are laterally shifted with respect to each other, such that the adjacent SrO layers adopt a rock salt-like structure. However, the similar thermodynamic stability of the neighboring RP-phases results in an abundance of isolated mono- and trilayers embedded in the bilayer matrix as shown by black arrows in Fig. 1(b). Furthermore, regions are found with high disorder due to $SrIrO_3$-like blocks [Fig. 1(c)].

Growth at a lower substrate temperature of 750 °C results in $SrIr_{1-\delta}O_3$ films, where δ denotes a slight iridium off-stoichiometry. As shown in Fig. 1(e), the crystal compensates for the iridium deficiency by arranging into distinct blocks of the perovskite phase, which are separated by highly ordered stacking faults. As highlighted in Fig. 1(f), these stacking faults correspond to the characteristic SrO double layers found in the RP structure and result in a similar spatial separation of 6.5 Å between adjacent IrO_2 layers as found in Sr_2IrO_4 and $Sr_3Ir_2O_7$.[34,35] While the out-of-plane XRD pattern in Fig. 1(g) corresponds to the cubic perovskite lattice despite the presence of stacking faults, the inherent disorder leads to some incoherence in the diffraction reflected in the absence of pronounced Laue oscillations in Fig. 1(h).

Upon further reduction in the substrate temperature, stoichiometric $SrIrO_3$ thin films are obtained. Figure 2(a) shows the intensity of the specular reflection high-energy electron diffraction (RHEED) signal during the growth of two equally thick $SrIrO_3$ films on TiO_2-terminated $SrTiO_3$. While the persistent intensity oscillations signal layer-by-layer film growth—where one oscillation is typically identified with the deposition of one monolayer—the observation of coherent RHEED patterns before and after deposition of $SrIrO_3$ (inset) evidences the high crystalline long-range order of the film surface. While the slightly different substrate temperatures (700–720 °C) and

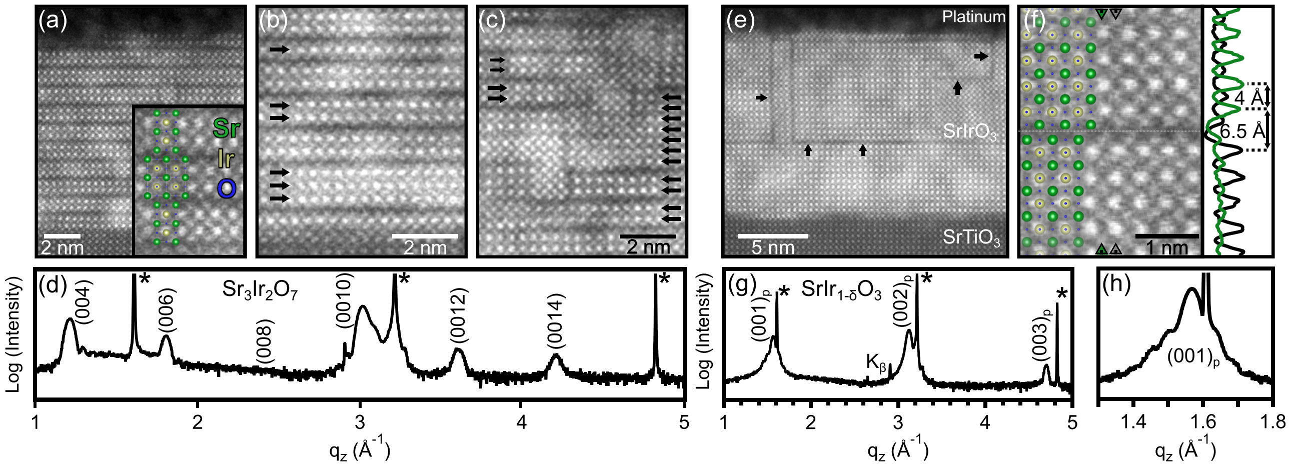

FIG. 1. (a) HAADF-STEM image of a $Sr_3Ir_2O_7$ film grown from a $SrIrO_3$ target. (b) RP-like stacking faults showing isolated mono- or trilayers embedded in a $Sr_3Ir_2O_7$ (i.e., bilayer) matrix. (c) Region with high disorder due to $SrIrO_3$-like blocks. (d) Out-of-plane XRD exhibits the $Sr_3Ir_2O_7$ pattern despite the abundance of lattice faults. Asterisks denote the diffraction from the $SrTiO_3$ substrate. (e) HAADF-STEM image of a slightly iridium-deficient $SrIr_{1-\delta}O_3$ film. Highly ordered stacking faults (arrows) divide the lattice into blocks of $SrIrO_3$. (f) The stacking faults consist of laterally shifted SrO double layers as found in the RP lattice structure. (g) Out-of-plane XRD exhibits a $SrIrO_3$ pattern with no other crystal phases present. (h) The present disorder reduces the coherence as reflected in the absence of Laue intensity oscillations in the diffraction signal from the film.

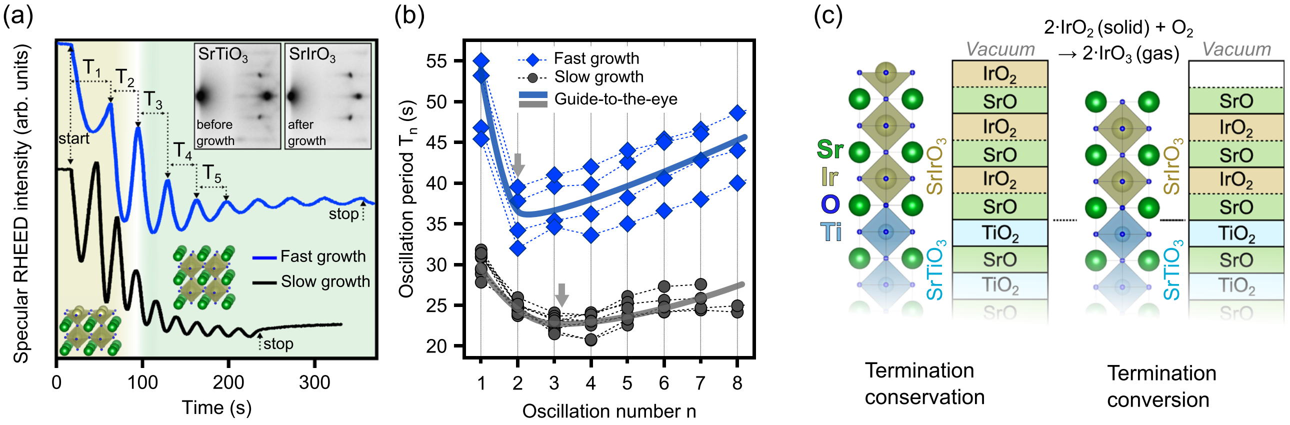

FIG. 2. (a) Specular RHEED intensity oscillations during the growth of SrIrO$_3$ in the temperature range of 700–720 °C at oxygen partial pressures of 0.05–0.08 mbar and different laser fluencies (slow growth: 1.7 J/cm^2; fast growth: 2.5 J/cm^2). Inset: RHEED patterns before and after deposition of SrIrO$_3$. (b) RHEED intensity oscillation period T_n as a function of oscillation number n. After one (three) prolonged oscillation period, a minimum is observed, followed by a gradual increase in T_n. (c) Preservation of the perovskite stacking and stoichiometric deposition would lead to an IrO$_2$ surface termination. Due to the volatility of IrO$_3$, a termination conversion to SrO-terminated SrIrO$_3$ occurs.

oxygen partial pressures (0.05–0.08 mbar) will influence the plume dynamics and hence the oxidative state of the iridium ions, the most pronounced effect is likely to be caused by the use of different laser fluencies (1.7 J/cm^2 and 2.5 J/cm^2), which results in significantly different growth rates.

Interestingly, the RHEED intensity oscillation period T_n of the nth oscillation does not remain constant throughout the deposition process, as shown in Fig. 2(b) for a selection of films grown at similar conditions. After a significantly prolonged first period, a minimal T_n is observed for the second ($n = 2$, blue) or third ($n \approx 3$, black) periods, followed by a gradual increase in T_n. The latter effect, i.e., a reduction in the deposition rate, is well-known and caused by an increasing reflectance of the target surface due to changes in the target surface morphology.[36–38] The prolonged first oscillation period bears a striking resemblance to the initial growth of SrRuO$_3$ on TiO$_2$-terminated SrTiO$_3$, where it is due to a deviation from the expected preservation of the perovskite stacking order AO-BO$_2$ in the (001) direction, which would result in a RuO$_2$-terminated surface.[39] Specifically, the topmost RuO$_2$ layer is unstable and forms volatile compounds until the terminating layer is completely converted into SrO. As evidenced by a doubling of the first oscillation period, for SrRuO$_3$, the conversion from A- to B-site termination is completed within the first unit cell at 700 °C and distributed over several oscillation periods at lower temperatures. We also note that the specular reflection of the RHEED patterns before and after growth [see the inset in Fig. 2(a)] exhibits a small intensity loss with respect to the (1, 0) and (−1, 0) reflections, which is reminiscent of the growth of SrRuO$_3$ and has been interpreted as a sign for termination conversion.[40]

We, hence, propose that a similar conversion from IrO$_2$ to SrO termination occurs during the growth of SrIrO$_3$ by over-oxidation of the terminating IrO$_2$ layer and subsequent evaporation of IrO$_3$. As shown in Fig. 2(c), the conservation of the perovskite stacking order on a TiO$_2$-terminated SrTiO$_3$ substrate results in a IrO$_2$-terminated surface with an incomplete IrO$_6$ octahedron. The tendency of BO$_2$-terminated perovskite transition metal oxides to adsorb excess oxygen ions at the apical site is well-documented.[41] We argue that the adsorption of an apical oxygen ion leads to the decomposition of the IrO$_6$ octahedron into gaseous molecular IrO$_3$ and the remaining SrO-terminated surface. Rather than the doubling of the first oscillation period as in the case of SrRuO$_3$, a prolongation of the first oscillation is observed experimentally during the growth of SrIrO$_3$. However, the minimal oscillation period consistently appears after a similar absolute time span (≈100 s) and independent of the growth rate, signaling that the IrO$_3$ formation and evaporation rate is only sensitive to the thermodynamic conditions to a good approximation.

As shown in Ref. 39, the characteristic, consistent signature of the RHEED intensity oscillations is a strong, but arguably indirect indication for a specific termination conversion. For more direct evidence, we investigated the microscopic surface structure of a 4 uc *thin* SrIrO$_3$ film, covered with a protective layer of amorphous carbon to facilitate the direct imaging of the surface by HAADF-STEM. The pronounced Laue oscillations and the STEM image of a *thick* film grown at identical conditions in Figs. 3(a) and 3(b) evidence the coherent growth of stoichiometric SrIrO$_3$ without stacking faults. Figure 3(c) shows an overview STEM image of the thin SrIrO$_3$ film, which, at the first glance, appears to be terminated by an IrO$_2$ layer. Indeed, the iridium columns (atomic number $Z = 77$) are most pronounced due to the Rutherford-like dependence of the scattering cross section in HAADF imaging ($\propto Z^n$ with $n \approx 1.7$),[42] followed by strontium ($Z = 38$) and titanium ($Z = 22$), while carbon and oxygen atoms are not detected. However, a signal is discerned above the topmost IrO$_2$ layer [cf. Fig. 3(d)], as highlighted by the averaged line profiles of the IrO$_2$/TiO$_2$ and SrO layers perpendicular to the surface (along $[001]_p$) in Fig. 3(e). The strong scattering from the heavy iridium atoms results in a broadened iridium signal, which overshadows the other atomic species. Nonetheless, the topmost atomic layer apparently stems from a SrO layer rather than an IrO$_2$ layer, as is suggested from the comparison of the SrO and IrO$_2$ line profiles with the last shoulder toward the surface seen for the former. For clarity, two horizontal line profiles of the subsurface (gray) and surface (green) SrO layer along the $[100]_p$ lattice direction are shown in Fig. 3(f). Despite the weak intensity of the surface layer, both signals clearly exhibit an in-phase periodicity that substantiates the conjecture of a SrO termination. Whether the weak signal strength of the terminating layer is exclusively caused by the

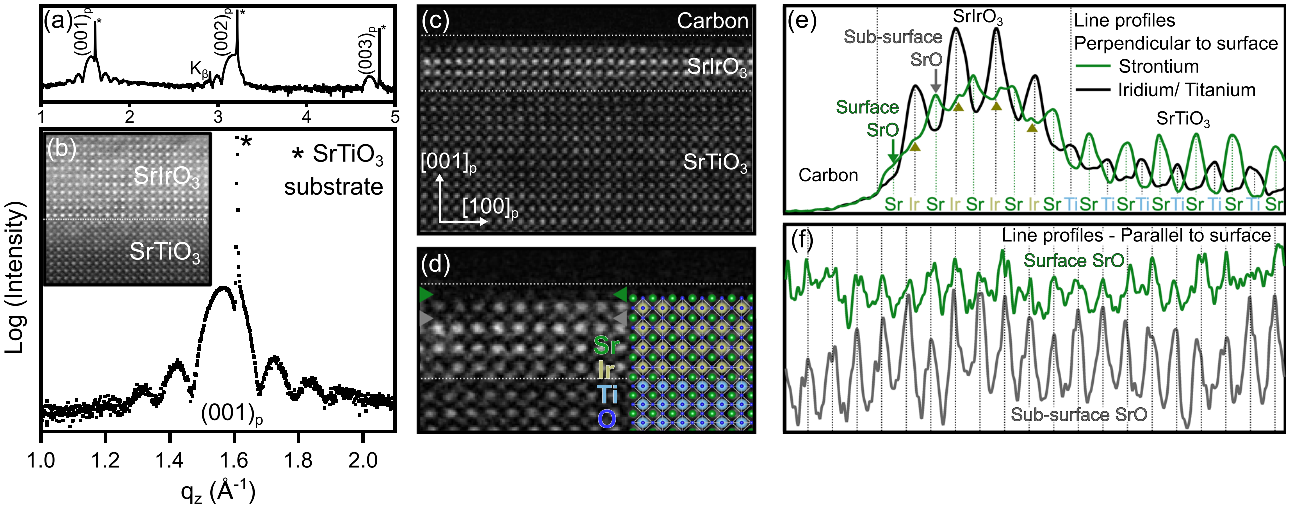

FIG. 3. (a) Out-of-plane XRD of a thick stoichiometric $SrIrO_3$ film. (b) Pronounced Laue fringes of the (001) diffraction peak signal a coherent film structure. Inset: HAADF-STEM image. (c) HAADF-STEM image of a thin $SrIrO_3$ film covered with amorphous carbon to facilitate the investigation of the surface. (d) Close-up of the film superimposed with a structural model. A faint terminating SrO layer can be discerned (green arrows). (e) Line profiles through the IrO_2/TiO_2 (black) and SrO (green) layers along the $[001]_p$ direction. In contrast to IrO_2, the SrO profile exhibits a shoulder at the film surface. (f) Line profiles of the surface- and sub-surface SrO layer along the $[100]_p$ direction. Both line profiles exhibit a clearly seen in-phase periodicity despite the small intensity of the terminating SrO layer.

broken translational symmetry at the surface or also due to an only partial, inhomogeneous SrO coverage of the sample remains an open question. Further investigations using atomic-resolution scanning probe techniques (e.g., scanning transmission or atomic force microscopy) may shed light on this in the future.

In the two-dimensional limit, the surface structure becomes critical for the electronic band structure because of the divergent surface-to-bulk ratio. Figure 4 compares the calculated DFT + U band structure of two supercells comprising four layers of $SrTiO_3$ and SrO- and IrO_2-terminated monolayers of $SrIrO_3$. For a realistic computation of the actual surface properties, a vacuum gap of 28.1 Å between adjacent supercells was introduced. Laterally, the supercells comprise two iridium sites to incorporate the collective octahedral rotations that enlarge the surface-projected unit cell of thin $SrIrO_3$ films by $\sqrt{2} \times \sqrt{2}$.[9] Note that the band structure is calculated for the enlarged unit cell (highlighted in red) and not backfolded into the pseudo-cubic

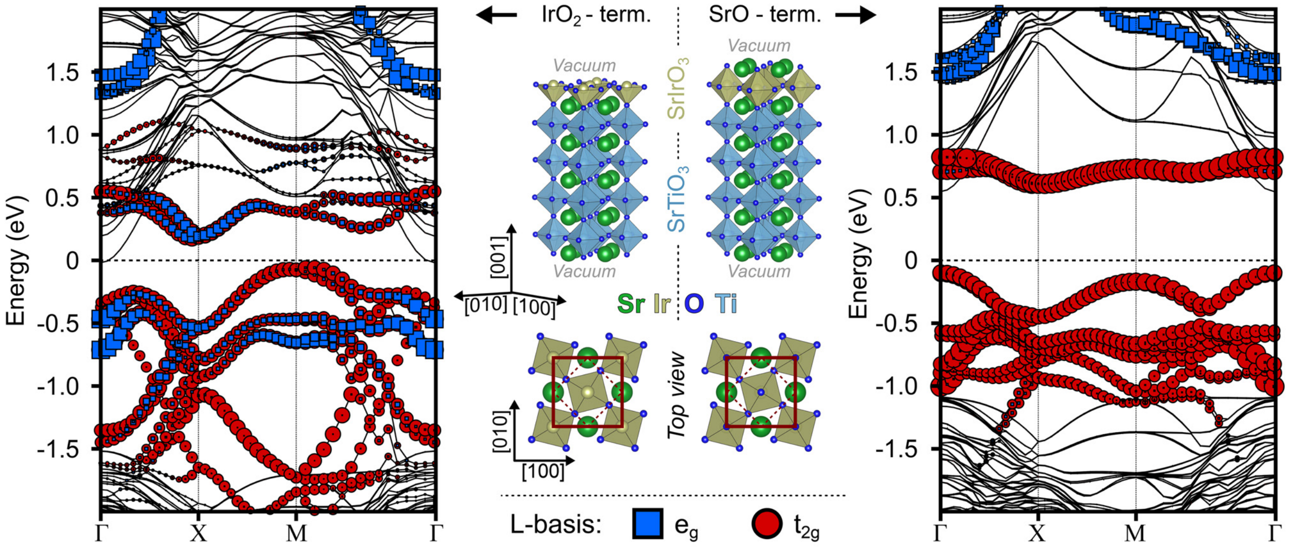

FIG. 4. DFT+U band structure calculations of two supercells comprising four unit cells of $SrTiO_3$ and a monolayer of $SrIrO_3$ with different terminations. The blue and red marker sizes indicate the e_g and t_{2g} orbital characteristics, respectively. Left: IrO_2-termination. Since the local O_h symmetry of the crystal field is broken, the e_g and t_{2g} states are mixed. Right: SrO-termination. The low-energy bands around the Fermi level are described by pure t_{2g} states as a consequence of the preserved O_h symmetry of the IrO_6 octahedra. The band structure is highly reminiscent of the bulk band structure of Sr_2IrO_4.

Brillouin zone (dashed red line), as in Ref. 9. Here, the sizes of the blue squares and red circles denote the Ir $5d$ e_g and t_{2g} orbital characteristics, respectively, as obtained from a projection onto the basis of the orbital angular momentum L.

The valence and conduction bands of the IrO_2-terminated monolayer in Fig. 4 exhibit a strong mixing of e_g and t_{2g} characteristics, whereas the SrO-termination results in a distinct separation thereof. Strictly speaking, the distinction between a t_{2g} and e_g manifold only holds in octahedral crystal fields with the point group symmetry O_h, which essentially originates from octahedra of negative point charges, i.e., the nearest-neighbor oxygen ligands in perovskite oxides. Hence, the observed orbital mixing occurs as a consequence of the broken local octahedral symmetry due to the absence of an apical oxygen at the IrO_2-terminated surface. In particular, the striking similarity between the electronic structure of $SrIrO_3$ in the monolayer limit and bulk Sr_2IrO_4[43,44] exclusively holds for SrO-terminated $SrIrO_3$. Hence, the observed self-organized conversion to a SrO termination is imperative for the close analogy between bulk Sr_2IrO_4 and monolayer $SrIrO_3$ since the quasi-two-dimensional network of fully closed IrO_6 octahedra constitutes their characteristic common structural feature.

In summary, the effects of iridium loss via the formation of volatile IrO_3 on the microstructure of strontium iridate films are investigated. While excessively oxidizing conditions may result in significant off-stoichiometry, even for nominally stoichiometric $SrIrO_3$, the terminating surface IrO_2 layer remains prone to over-oxidation. The consequential conversion from B- to A-site termination is evidenced by direct surface imaging using scanning transmission electron microscopy and found to strongly influence the electronic structure of $SrIrO_3$ thin films. The local octahedral symmetry in SrO-terminated $SrIrO_3$ monolayers restores the crystal field splitting of e_g and t_{2g} states and results in an electronic structure similar to bulk Sr_2IrO_4. With regard to $SrIrO_3$ as a potential topologically non-trivial metal, these findings are relevant for further theoretical predictions of symmetry-protected zero-energy surface states.

We acknowledge the financial support from the DFG through the Würzburg-Dresden Cluster of Excellence on Complexity and Topology in Quantum Matter "ct.qmat" (EXC 2147, Project ID. 39085490) as well as through the Collaborative Research Center SFB 1170 "ToCoTronics" (Project ID 258499086). The authors gratefully acknowledge the Gauss Center for Supercomputing e.V. for providing computing time on the GCS Supercomputer SuperMUC at the Leibniz Supercomputing Center (LRZ).

REFERENCES

[1] W. Witczak-Krempa, G. Chen, Y. B. Kim, and L. Balents, Annu. Rev. Condens. Matter Phys. **5**, 57 (2014).

[2] G. Jackeli and G. Khaliullin, Phys. Rev. Lett. **102**, 017205 (2009).

[3] B. J. Kim, H. Ohsumi, T. Komesu, S. Sakai, T. Morita, H. Takagi, and T. Arima, Science **323**, 1329 (2009).

[4] Y. K. Kim, O. Krupin, J. D. Denlinger, A. Bostwick, E. Rotenberg, Q. Zhao, J. F. Mitchell, J. W. Allen, and B. J. Kim, Science **345**, 187 (2014).

[5] Y. K. Kim, N. H. Sung, J. D. Denlinger, and B. J. Kim, Nat. Phys. **12**, 37 (2016).

[6] J. M. Longo, J. A. Kafalas, and R. J. Arnott, J. Solid State Chem. **3**, 174 (1971).

[7] J. G. Zhao, L. X. Yang, Y. Yu, F. Y. Li, R. C. Yu, Z. Fang, L. C. Chen, and C. Q. Jin, J. Appl. Phys. **103**, 103706 (2008).

[8] Y. F. Nie, P. D. C. King, C. H. Kim, M. Uchida, H. I. Wei, B. D. Faeth, J. P. Ruf, J. P. C. Ruff, L. Xie, X. Pan, C. J. Fennie, D. G. Schlom, and K. M. Shen, Phys. Rev. Lett. **114**, 016401 (2015).

[9] P. Schütz, D. Di Sante, L. Dudy, J. Gabel, M. Stübinger, M. Kamp, Y. Huang, M. Capone, M.-A. Husanu, V. N. Strocov, G. Sangiovanni, M. Sing, and R. Claessen, Phys. Rev. Lett. **119**, 256404 (2017).

[10] J.-M. Carter, V. V. Shankar, M. A. Zeb, and H.-Y. Kee, Phys. Rev. B **85**, 115105 (2012).

[11] Y. Chen, Y.-M. Lu, and H.-Y. Kee, Nat. Commun. **6**, 6593 (2015).

[12] D. J. Groenendijk, C. Autieri, J. Girovsky, M. C. Martinez-Velarte, N. Manca, G. Mattoni, A. M. R. V. L. Monteiro, N. Gauquelin, J. Verbeeck, A. F. Otte, M. Gabay, S. Picozzi, and A. D. Caviglia, Phys. Rev. Lett. **119**, 256403 (2017).

[13] J. M. Huijbregtse, B. Dam, J. H. Rector, and R. Griessen, J. Appl. Phys. **86**, 6528 (1999).

[14] T. Ohnishi, M. Lippmaa, T. Yamamoto, S. Meguro, and H. Koinuma, Appl. Phys. Lett. **87**, 241919 (2005).

[15] T. Ohnishi, K. Shibuya, T. Yamamoto, and M. Lippmaa, J. Appl. Phys. **103**, 103703 (2008).

[16] J. H. Song, T. Susaki, and H. Y. Hwang, Adv. Mater. **20**, 2528 (2008).

[17] H. K. Sato, C. Bell, Y. Hikita, and H. Y. Hwang, Appl. Phys. Lett. **102**, 251602 (2013).

[18] A. Ohtomo, D. A. Muller, J. L. Grazul, and H. Y. Hwang, Appl. Phys. Lett. **80**, 3922 (2002).

[19] Y. Hotta, Y. Mukunoki, T. Susaki, H. Y. Hwang, L. Fitting, and D. A. Muller, Appl. Phys. Lett. **89**, 031918 (2006).

[20] P. Scheiderer, M. Schmitt, J. Gabel, M. Zapf, M. Stübinger, P. Schütz, L. Dudy, C. Schlueter, T.-L. Lee, M. Sing, and R. Claessen, Adv. Mater. **30**, 1706708 (2018).

[21] W. E. Bell and M. Tagami, J. Phys. Chem. **67**, 2432 (1963).

[22] E. H. P. Cordfunke and G. Meyer, Recl. Trav. Chim. Pays-Bas **81**, 495 (2010).

[23] E. H. P. Cordfunke and G. Meyer, Recl. Trav. Chim. Pays-Bas **81**, 670 (2010).

[24] T. Ohnishi and K. Takada, Appl. Phys. Express **4**, 025501 (2011).

[25] K. Nishio, H. Y. Hwang, and Y. Hikita, APL Mater. **4**, 036102 (2016).

[26] M. Kawasaki, K. Takahashi, T. Maeda, R. Tsuchiya, M. Shinohara, O. Ishiyama, T. Yonezawa, M. Yoshimoto, and H. Koinuma, Science **266**, 1540 (1994).

[27] G. Koster, B. L. Kropman, G. J. H. M. Rijnders, D. H. A. Blank, and H. Rogalla, Appl. Phys. Lett. **73**, 2920 (1998).

[28] G. Kresse and J. Furthmüller, Phys. Rev. B **54**, 11169 (1996).

[29] P. E. Blöchl, Phys. Rev. B **50**, 17953 (1994).

[30] G. Kresse and D. Joubert, Phys. Rev. B **59**, 1758 (1999).

[31] J. P. Perdew, K. Burke, and M. Ernzerhof, Phys. Rev. Lett. **77**, 3865 (1996).

[32] S. Steiner, S. Khmelevskyi, M. Marsmann, and G. Kresse, Phys. Rev. B **93**, 224425 (2016).

[33] A. I. Liechtenstein, Phys. Rev. B **52**, R5467 (1995).

[34] F. Ye, S. Chi, B. C. Chakoumakos, J. A. Fernandez-Baca, T. Qi, and G. Cao, Phys. Rev. B **87**, 140406 (2013).

[35] T. Hogan, L. Bjaalie, L. Zhao, C. Belvin, X. Wang, C. G. Van de Walle, D. Hsieh, and S. D. Wilson, Phys. Rev. B **93**, 134110 (2016).

[36] S. R. Foltyn, R. C. Dye, K. C. Ott, E. Peterson, K. M. Hubbard, W. Hutchinson, R. E. Muenchausen, R. C. Estler, and X. D. Wu, Appl. Phys. Lett. **59**, 594 (1991).

[37] J.-S. Chung, S. Y. Jang, S. J. Moon, and B. C. Jeon, J. Korean Phys. Soc. **56**, 1814 (2010).

[38] D. J. Groenendijk, N. Manca, G. Mattoni, L. Kootstra, S. Gariglio, Y. Huang, E. van Heumen, and A. D. Caviglia, Appl. Phys. Lett. **109**, 041906 (2016).

[39] G. Rijnders, D. H. A. Blank, J. Choi, and C.-B. Eom, Appl. Phys. Lett. **84**, 505 (2004).

[40] G. Koster, L. Klein, W. Siemons, G. Rijnders, J. S. Dodge, C.-B. Eom, D. H. A. Blank, and M. R. Beasley, Rev. Mod. Phys. **84**, 253 (2012).

[41] Y. Okada, S.-Y. Shiau, T.-R. Chang, G. Chang, M. Kobayashi, R. Shimizu, H.-T. Jeng, S. Shiraki, H. Kumigashira, A. Bansil, H. Lin, and T. Hitosugi, Phys. Rev. Lett. **119**, 086801 (2017).

[42] P. Hartel, H. Rose, and C. Dinges, Ultramicroscopy **63**, 93 (1996).

[43] B. Kim, H. Jin, S. Moon, J.-Y. Kim, B.-G. Park, C. Leem, J. Yu, T. Noh, C. Kim, S.-J. Oh, J.-H. Park, V. Durairaj, G. Cao, and E. Rotenberg, Phys. Rev. Lett. **101**, 076402 (2008).

[44] H. Zhang, K. Haule, and D. Vanderbilt, Phys. Rev. Lett. **111**, 246402 (2013).